

HiMoR: Monocular Deformable Gaussian Reconstruction with Hierarchical Motion Representation

Yiming Liang^{1*} Tianhan Xu² Yuta Kikuchi²

¹ Waseda University ² Preferred Networks, Inc.

yiming.liang@toki.waseda.jp, {xutianhan, kikuchi}@preferred.jp

Abstract

We present *Hierarchical Motion Representation (HiMoR)*, a novel deformation representation for 3D Gaussian primitives capable of achieving high-quality monocular dynamic 3D reconstruction. The insight behind HiMoR is that motions in everyday scenes can be decomposed into coarser motions that serve as the foundation for finer details. Using a tree structure, HiMoR’s nodes represent different levels of motion detail, with shallower nodes modeling coarse motion for temporal smoothness and deeper nodes capturing finer motion. Additionally, our model uses a few shared motion bases to represent motions of different sets of nodes, aligning with the assumption that motion tends to be smooth and simple. This motion representation design provides Gaussians with a more structured deformation, maximizing the use of temporal relationships to tackle the challenging task of monocular dynamic 3D reconstruction. We also propose using a more reliable perceptual metric as an alternative, given that pixel-level metrics for evaluating monocular dynamic 3D reconstruction can sometimes fail to accurately reflect the true quality of reconstruction. Extensive experiments demonstrate our method’s efficacy in achieving superior novel view synthesis from challenging monocular videos with complex motions.

1. Introduction

Dynamic 3D scene reconstruction aims to recover the geometry, appearance, and motion of dynamic scenes from video data. The reconstructed dynamic 3D model allows free-viewpoint rendering at any timestep, enabling practical applications in virtual reality, video production, and even provides an innovative way for individuals to capture and relive their memorable moments.

With the recent rise of research on 3D Gaussian Splatting (3DGS) [17], some methods attempt to reconstruct dynamic 3D scenes from multi-view videos by jointly learning

Gaussians and their deformations [29, 52]. However, reconstruction from a monocular video remains particularly challenging due to the limited available information, especially the lack of a multi-view consistency constraint. Recent works focus on designing deformation models for Gaussians that can better integrate temporal information across frames, overcoming the limited available information in monocular videos. For instance, Shape of Motion (SoM) [48] introduces a set of global motion bases, assigning each Gaussian coefficients that determine its motion, based on the insight that motion is generally smooth and simple, or in other words, low-rank. As the entire scene shares a limited number of global motion bases, capturing fine motion details becomes difficult. Another representative work MoSca [15] models motion using hundreds of 3D nodes, with each Gaussian interpolating its deformation from surrounding nodes. Such a large number of motion nodes brings a high degree of freedom, making optimization prone to overfit to the training view. Similar challenges are faced by other works [26, 44, 49, 56], where methods either struggle to capture fine details or suffer from overfitting, hindering high-quality reconstruction with smooth motion in both spatial and temporal dimensions.

To tackle the aforementioned issue, we propose a novel hierarchical motion representation that captures motion at both coarse and fine levels. This approach enables high-quality monocular reconstruction of dynamic 3D scenes, maintaining both spatio-temporal consistency and fine details. Specifically, our hierarchical motion representation is implemented through a tree structure, where each node represents relative motion w.r.t. its parent node. The global motion w.r.t. the world coordinate can be iteratively derived from the hierarchy of the tree structure, assuming the root node is stationary at the origin of the world coordinate. This design allows nodes at different levels (*i.e.*, tree depth) to express motions at different levels of detail, enabling the decomposition of coarse and fine motion.

The insight behind our approach is that, in everyday life scenarios, finer motions tend to be associated with coarser motions. For instance, the movement of fingers can be bro-

*Work was done during an internship at Preferred Networks, Inc..

ken down into the fine motion of fingers relative to the wrist, combined with the coarse motion of the arm. The benefit of this decomposition is that it not only makes learning complex motions easier but also leads to a more reasonable motion representation: coarser motion effectively captures spatial and temporal smoothness, while finer motion enriches the expression of details.

In addition, from an evaluation perspective, we find that due to the highly ill-posed nature of monocular dynamic scene reconstruction, commonly used pixel-level metrics (e.g., PSNR) are susceptible to factors such as depth ambiguity or inaccurate camera parameter estimation. As a result, they sometimes fail to intuitively reflect the reconstruction quality due to pixel misalignment. Therefore, we propose using a perceptual metric for evaluating rendering quality. Quantitative results also demonstrate that the perceptual metric aligns more closely with human perception.

We evaluated our proposed method on multiple standard benchmarks, demonstrating its superiority over existing methods both qualitatively and quantitatively. Notably, our method made significant improvements in the spatio-temporal smoothness of the motion and the restoration of details. To summarize, our contributions are as follows:

- We propose a novel hierarchical motion representation that decomposes complex motion into smooth coarse motion and detailed fine motion. This provides Gaussians with more structured deformations, leading to an enhanced representation of dynamic 3D scenes.
- We identify the limitations of existing pixel-level metrics for evaluating the rendering quality of monocular dynamic scene reconstruction and propose the use of more appropriate perceptual metrics for evaluation.
- We achieve state-of-the-art results both qualitatively and quantitatively.

2. Related work

2.1. Novel view synthesis

Neural Radiance Field (NeRF) [30] has revolutionized the field of novel view synthesis. NeRF leverages coordinate-based multi-layer perceptrons (MLPs) to implicitly represent a scene as a field of color and density. While subsequent works have flourished in various areas [1, 6, 11, 16, 20, 25, 32, 35, 46, 53, 59], its rendering efficiency remains a challenge due to the fundamentally computationally intensive rendering formulation.

Recently, 3D Gaussian Splatting (3DGS) [17] has received considerable attention. Its novel scene representation with 3D Gaussian primitives, combined with an efficient rasterization-based renderer, achieves real-time rendering while maintaining or even surpassing NeRF’s quality. Subsequent works have further extended the capability of 3DGS in quality [13, 18, 27, 31, 60], efficiency [7, 10, 27, 33], gen-

eralizability [2, 4, 45], and editability [3, 57].

While the original NeRF and 3DGS aim to reconstruct static scenes, as we detail below, combining 3D representation with motion allows for a natural extension to dynamic 3D scene reconstruction.

2.2. Dynamic 3D scene reconstruction

Dynamic 3D scene reconstruction aims to recover the time-varying geometry, appearance, and motion of scenes from video observations. Some recent works utilizing videos captured by multiple synchronized cameras aim to achieve high-quality reconstruction results [8, 22, 24, 29, 38, 47, 52]. Meanwhile, other methods focus on reconstruction from monocular video, which is more closely aligned with real-world application settings [9, 15, 23, 26, 36, 37, 44, 48, 49, 56]. The essence of most methods lies in using a reasonable motion representation to deform a 3D representation, thus obtaining a dynamic scene. This strategy effectively leverages temporal sequence information, simplifying the challenging task of monocular reconstruction. For specific scene categories, predefined templates are often used as priors for motion representation [12, 42, 51]. For general dynamic scenes, NeRF-based approaches usually learn a deformation field alongside a color and density field. This field is used to warp the scene from the canonical frame to each observation frame, an idea that naturally stems from NeRF’s neural field representation [9, 36, 37]. Due to the smoothness property of MLPs, deformation fields implemented by MLPs can effectively represent continuous motion but often struggle to model detailed motion. Some methods based on 3DGS also rely on the deformation field [26, 39, 56]. Despite 3DGS’s inherent efficiency and high-quality rendering, such combinations can still be hindered by the slow computation and oversmoothing problems associated with the deformation field. Other 3DGS-based methods explicitly model a motion sequence to represent deformation instead of relying on an MLP-based implicit field. For example, [21, 48] leverage a set of globally shared motion bases to constrain the deformation field, while [15] deforms Gaussians via a sparse motion scaffold graph, ensuring spatial smoothness.

As mentioned above, motion representation plays a crucial role in monocular dynamic 3D scene reconstruction, and there remains room for improvement in modeling detailed motion while maintaining temporal consistency.

3. Method

Given a monocular video with calibrated camera parameters that represents a dynamic scene, our goal is to reconstruct a dynamic 3DGS representation, which includes canonical Gaussians and motion sequences used for their deformation.

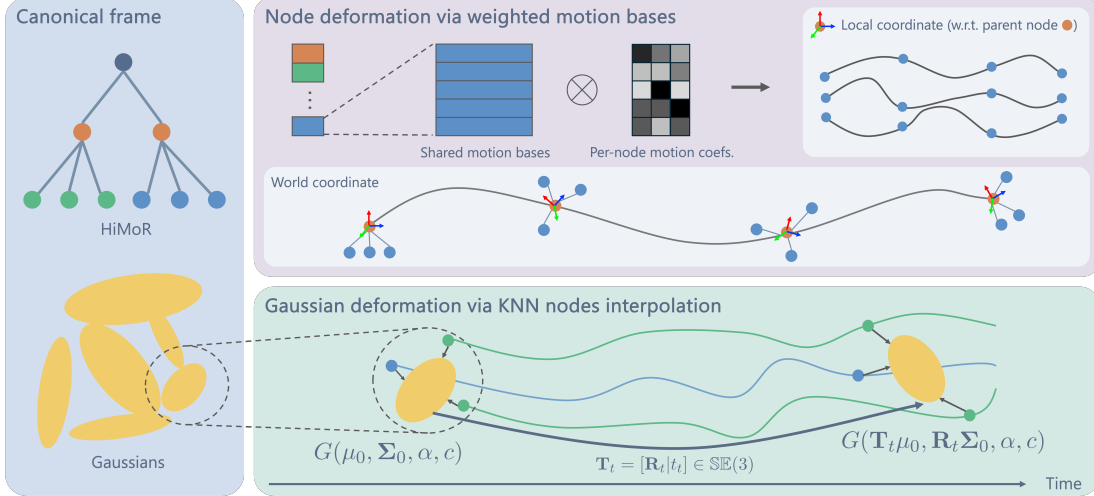


Figure 1. **Overview.** **Left:** The proposed hierarchical motion representation (HiMoR) is defined in the canonical frame with 3D Gaussian primitives. HiMoR uses a tree structure where each node represents the relative motion to its parent node, with the root node representing stationary motion that is fixed to the world coordinate origin. **Top right:** Child nodes that belong to the same parent node share a set of $\mathbb{SE}(3)$ motion bases, and the motion of each child node is obtained by weighting the motion bases with its own coefficients. The motion of leaf nodes relative to the world coordinate is iteratively computed based on the hierarchy of HiMoR. **Bottom right:** The deformation of each Gaussian is derived by weighting the motion of its K-nearest neighbor (KNN) leaf nodes within the canonical frame.

3.1. Preliminary: 3D Gaussian Splatting

3DGS [17] represents a static scene with a set of anisotropic 3D Gaussian primitives, which enables real-time photo-realistic rendering. Each 3D Gaussian primitive $G(\boldsymbol{\mu}, \boldsymbol{\Sigma}, \alpha, \mathbf{c})$ is parameterized by a mean $\boldsymbol{\mu} \in \mathbb{R}^3$, a covariance matrix $\boldsymbol{\Sigma} \in \mathbb{R}^{3 \times 3}$, an opacity $\alpha \in \mathbb{R}^+$, and a view-dependent color determined by spherical harmonics (SH) coefficients $\mathbf{c} \in \mathbb{R}^{3(l+1)^2}$, where l denotes the degree of SH coefficients. To render 3D Gaussians $\{G_k\}$ from a camera parameterized by θ , each 3D Gaussian is first splatted to 2D Gaussian with mean $\boldsymbol{\mu}' = \Pi(\boldsymbol{\mu}; \theta) \in \mathbb{R}^2$ and covariance $\boldsymbol{\Sigma}' = \Pi(\boldsymbol{\Sigma}; \theta) \in \mathbb{R}^{2 \times 2}$ at the image plane, where Π denotes camera projection. Then, the 2D Gaussians are sorted by depth from the camera and rendered via alpha blending with an efficient differentiable rasterizer as follows:

$$\mathbf{C}(\mathbf{p}) = \sum_{i=1}^N c_i \sigma_i(\mathbf{p}) \left(\prod_{j=1}^{i-1} (1 - \sigma_j(\mathbf{p})) \right),$$

$$\sigma_i(\mathbf{p}) = \alpha_i \exp \left(-\frac{1}{2} (\mathbf{p} - \boldsymbol{\mu}'_i)^T (\boldsymbol{\Sigma}'_i)^{-1} (\mathbf{p} - \boldsymbol{\mu}'_i) \right), \quad (1)$$

where $\mathbf{p} \in \mathbb{R}^2$ is the 2D coordinate of the queried pixel, and N is the number of Gaussians that intersect the ray corresponding to the pixel.

To extend 3DGS to dynamic scenes, deformations are applied to the Gaussians to transform them from a static canonical frame to target frames, leading to a dynamic Gaussian representation. Assuming $\mathbf{T}_t = [\mathbf{R}_t | \mathbf{t}_t] \in \mathbb{SE}(3)$

as the deformation of a Gaussian $G(\boldsymbol{\mu}_0, \boldsymbol{\Sigma}_0, \alpha, \mathbf{c})$ from the canonical frame to the target frame t . The deformed Gaussian at t is then derived as $G(\mathbf{T}_t \boldsymbol{\mu}_0, \mathbf{R}_t \boldsymbol{\Sigma}_0, \alpha, \mathbf{c})$. We treat α and \mathbf{c} remaining unchanged over time.

3.2. Hierarchical motion representation

The core of our approach is a hierarchical motion representation (HiMoR) that deforms 3D Gaussians for dynamic 3D scene reconstruction. Specifically, HiMoR is a tree graph, where each node represents the relative $\mathbb{SE}(3)$ motion sequence w.r.t. its parent node. The deformation of a 3D Gaussian is derived as the weighted sum of motions from its nearby leaf nodes.

3.2.1 Formulation

We first introduce the formulation of HiMoR. The nodes in HiMoR represent a sequence of $\mathbb{SE}(3)$ over a time series T :

$$\mathcal{D} = \{\mathbf{D}_t\}_{t=1}^T, \quad (2)$$

where $\mathbf{D}_t \in \mathbb{SE}(3)$ denotes the transformation of a node from the canonical frame to frame t . While it could be straightforward to assign an individual motion sequence to each node, as done in MoSca [15], we consider the low-rank assumption of motion [21, 48] and propose using shared motion bases to model the motion of the nodes.

Here, a motion base represents a sequence of $\mathbb{SE}(3)$ transformations as $\mathcal{B} = \{\mathbf{B}_t\}_{t=1}^T$, where $\mathbf{B}_t \in \mathbb{SE}(3)$. Our

aim is to represent the target $\mathbb{SE}(3)$ motion sequence by a weighted sum of a set of motion bases. Specifically, consider a parent node with N child nodes. We employ a set of M motion bases $\{\mathcal{B}_m\}_{m=1}^M$, where each child node owns coefficients $\{v_m\}_{m=1}^M$, where $v_m \in \mathbb{R}$, to weight these motion bases. With a slight abuse of notation, the motion of a node is expressed as the linear combination of motion bases:

$$\mathcal{D} = \sum_{m=1}^M v_m \mathcal{B}_m. \quad (3)$$

This formulation is defined recursively, with the motion of the root node set to the origin of the world coordinate (*i.e.*, a time-invariant identity matrix). To provide a more detailed explanation, when a node serves as a parent, it is equipped with a set of motion bases to model the motion of its child nodes; when a node acts as a child, it is assigned coefficients to interpolate the motion bases of its parent node. Within HiMoR, the root node only serves as a parent node, and leaf nodes only act as child nodes, while all other intermediate nodes serve as both parent and child nodes.

Note that due to the hierarchical nature of HiMoR, each node’s motion represents its relative motion to its parent node, rather than its absolute motion relative to the world coordinate. This modeling allows the motion to be decomposed into coarse parts (represented by shallow nodes) and fine ones (represented by deep nodes). The coarse-to-fine design retains the ability to represent details while simplifying the process of learning complex motions. The global motion of each node relative to the world coordinate can be obtained by composing $\mathbb{SE}(3)$ transformations according to the kinematic chain of HiMoR.

The motivation behind the proposed HiMoR is two-fold: 1) Motion can often be decomposed into coarse, detailed, and even more detailed components. Therefore, we employ the hierarchical tree structure for its coarse-to-fine modeling capabilities, allowing us to capture more refined motion details at deeper levels; 2) Motion is typically low-rank, and the motion of neighboring regions tends to be similar, which leads us to model with a limited number of motion bases and nodes.

3.2.2 Deforming Gaussians with HiMoR

Given the formulation of HiMoR discussed above, we can compute the motion sequence of all nodes. For non-leaf nodes (those with child nodes), their motion sequences provide a relatively rough motion foundation for the finer nodes at the next level; whereas for leaf nodes possessing the finest motion, we use them to guide the deformation of the 3D Gaussians. Specifically, the deformation $\mathcal{T} = \{\mathbf{T}_t\}_{t=1}^T$ of a Gaussian G is interpolated from the leaf nodes \mathcal{V} as:

$$\mathcal{T} = \sum_{k \in \mathcal{N}(G, \mathcal{V})} w_k \mathcal{D}_k. \quad (4)$$

Each node in HiMoR is associated with a position $\mathbf{x} \in \mathbb{R}^3$ in the canonical frame, and a radius $r \in \mathbb{R}^+$ that controls its influence range. $\mathcal{N}(G, \mathcal{V})$ denotes the indices of the K-nearest neighbor (KNN) leaf nodes to G in terms of Euclidean distance. $w_k \in \mathbb{R}^+$ is the skinning weight, which is a function of the Gaussian center $\boldsymbol{\mu}$ and is calculated from Gaussian function as:

$$w_k(\boldsymbol{\mu}) = \frac{1}{Z} \exp\left(-\frac{\|\boldsymbol{\mu} - \mathbf{x}_k\|^2}{2r_k}\right), \quad (5)$$

where $Z \in \mathbb{R}^+$ is a normalization term. Additionally, we use dual quaternion as [34] for better interpolation quality.

Differ from methods [28, 48, 56] modeling the deformation for each Gaussian, interpolating from motion nodes can make the deformation field become more spatially smooth. Meanwhile, motion nodes can receive gradients from surrounding Gaussians over a larger area, making the deformation optimization more stable.

3.2.3 Initialization

Given that monocular dynamic 3D scene reconstruction is highly ill-posed, we follow previous works [15, 48], leveraging pretrained models (*e.g.*, 2D tracking [5], depth estimation [55]) for the initialization of HiMoR. At the beginning of the optimization, HiMoR initially has only one level (*i.e.*, the orange nodes in Fig. 1, with the root node as their parent). As optimization progresses, the levels of HiMoR gradually increase.

Here, the initialization determines the motion bases shared by the first-level nodes (*i.e.*, attached to the root nodes) and the coefficients of each first-level node. We start by unprojecting 2D tracks of the foreground using metric-aligned relative depth maps to obtain 3D tracks. Next, we apply K-Means clustering to the 3D tracks, obtaining M clusters, and use their centers to define M 3D trajectories. Since these trajectories include only translation (*i.e.*, \mathbb{R}^3 sequence) and lack orientation, we solve the Procrustes problem over time for each cluster to obtain M $\mathbb{SE}(3)$ sequences that serve as motion bases. Then, we select the frame with the highest number of visible 3D tracks as the canonical frame. Finally, we sample node positions from the 3D tracks in the canonical frame and initialize the coefficients for motion bases according to the distance from the position of the motion bases (*i.e.*, the cluster centers) in the canonical frame using inverse distance weighting.

Nodes at the finer level are added gradually during the optimization in an iterative manner. The specific operation is similar to the initialization of the first-level nodes mentioned above: for each leaf node, we first select Gaussians within a certain radius and calculate their relative motion w.r.t. this leaf node. Then, we cluster these relative motions into M clusters through K-Means, with the center motion of

each cluster serving as the motion basis. The child nodes are subsampled from the surrounding Gaussians, and the initial coefficients are derived based on their distance to the center of the motion bases. The main difference from the initialization of the first-level nodes is that K-Means is applied to oriented Gaussians, meaning that the resulting cluster center sequences already contain orientation information, thus eliminating the need to solve the Procrustes problem.

3.2.4 Node densification

As the nodes of HiMoR are solely initialized by the visible 3D tracks in the canonical frame, they cannot effectively model the motion of invisible regions within that frame. Therefore, a progressive node densification strategy is needed to capture the entire motion within the scene. In the context of Gaussian densification in 3DGS [17], additional Gaussians are incorporated based on the gradient of photometric loss. Previous work that employs motion nodes similar to ours [14] also used a gradient-based method for node densification. However, we found that relying solely on this approach may not always yield meaningful nodes. For instance, areas with relatively uniform color but sparse nodes may not get additional nodes, hindering a detailed representation of motion in that area. To overcome this, we propose a more intuitive node densification strategy: for each Gaussian, if its surrounding nodes are too sparse to provide it with meaningful motion interpolation, we add new nodes around it. Specifically, we measure node density around the Gaussian by calculating curve distance between the trajectories of the Gaussian and its KNN motion nodes. Following [15], the curve distance between the trajectories of two points is defined as the maximum distance between the points over time:

$$d_{\text{curve}}(\mathcal{X}, \mathcal{Y}) = \max_{t=1 \dots T} \|\mathbf{x}_t - \mathbf{y}_t\|, \quad (6)$$

where the trajectories $\mathcal{X} = \{\mathbf{x}_t\}_{t=1}^T$ and $\mathcal{Y} = \{\mathbf{y}_t\}_{t=1}^T$ denote \mathbb{R}^3 sequences, and $\|\cdot\|$ means Euclidean norm. Then, we sample new motion nodes among Gaussians with curve distance above a threshold.

We periodically apply this densification strategy at the beginning of the optimization, and after a certain number of steps, we add or prune nodes based on the gradient of the surrounding Gaussians, as proposed in [14], for further refinement.

3.3. Loss design

3.3.1 Rigidity loss

Rigidity loss constrains deformation by limiting the changes in displacement, velocity, *etc.*, in neighboring areas, thus ensuring locally rigid motion and better overall preservation of geometry. Previous works [14, 15, 28, 44]

have adopted such a rigidity loss to constrain motion. However, they often face a dilemma: too weak a constraint might not function effectively, potentially causing the motion to disperse, while too strong a constraint may suppress the representation of detailed motion.

With HiMoR’s hierarchical structure, we address this by applying different levels of constraints based on node level. Specifically, stronger constraints are imposed on shallower nodes to enforce smoother, coarser motion, while deeper nodes receive weaker constraints, allowing for greater flexibility in capturing fine-grained motion. The hierarchical structure, combined with the varied intensity of rigidity constraints, achieves a coarse-to-fine decomposition of motion.

3.3.2 Overall loss

We integrate the knowledge from pre-trained models into the optimization process through loss function to mitigate the ill-posed nature of reconstruction from a monocular video. The loss function consists of multiple terms: the traditional rendering loss \mathcal{L}_{rgb} , the foreground masks loss \mathcal{L}_{mask} , the depth loss \mathcal{L}_{depth} , the tracking loss \mathcal{L}_{track} , and the rigidity loss \mathcal{L}_{rigid} . For \mathcal{L}_{mask} , we use foreground masks produced by a segmentation model [54] as ground truth. The ground truth for \mathcal{L}_{depth} is a relative depth map predicted by a monocular depth estimation model [55] aligned with either Lidar depth or the depth from COLMAP [41]. To better recover the motion, we also adopt tracking loss \mathcal{L}_{track} that penalizes the difference between the rendered tracks and the tracks predicted by pre-trained 2D tracking model [5]. In combination with \mathcal{L}_{rigid} described above, the overall loss can be written as:

$$\mathcal{L}_{total} = \lambda_{rgb}\mathcal{L}_{rgb} + \lambda_{mask}\mathcal{L}_{mask} + \lambda_{depth}\mathcal{L}_{depth} + \lambda_{track}\mathcal{L}_{track} + \lambda_{rigid}\mathcal{L}_{rigid}. \quad (7)$$

The Gaussians in the canonical frame and HiMoR are optimized jointly with \mathcal{L}_{total} .

4. Experiments

Implementation detail. As illustrated in Fig. 1, we use a two-layer HiMoR (excluding the root node). The first layer initializes 50 nodes to share 10 motion bases. After certain optimization/densification steps, each node in the first layer spawns 10 child nodes sharing 5 motion bases.

Datasets. We evaluate our method on the iPhone dataset [9] and the Nvidia dataset [43]. The iPhone dataset includes 14 scenes, 7 of which feature multi-camera captures for the evaluation of novel view synthesis. We follow the settings in [48], using five scenes and excluding the other two with camera inaccuracies. The Nvidia dataset consists of seven scenes captured with a rig with 12 cameras. Following [44], we perform evaluation under a strict monocular setting, using video from camera 4 for training and camera 3, 5, and 6

Method	Apple				Block				Paper-windmill			
	CLIP-I \uparrow	CLIP-T \uparrow	LPIPS \downarrow	PCK-T \uparrow	CLIP-I \uparrow	CLIP-T \uparrow	LPIPS \downarrow	PCK-T \uparrow	CLIP-I \uparrow	CLIP-T \uparrow	LPIPS \downarrow	PCK-T \uparrow
T-NeRF [9]	0.8275	0.9729	0.6695	-	0.8873	0.9749	0.4729	-	0.9304	0.9858	0.4837	-
HyperNeRF [37]	0.8314	0.9771	0.6626	0.3183	0.8882	0.9756	0.4654	0.2146	0.9218	0.9818	0.4319	0.1074
Deformable 3DGS [56]	0.7822	0.9730	0.8558	0.2412	0.8105	0.9720	0.7281	0.1651	0.8652	0.9814	0.6411	0.1583
Marbles [44]	0.8055	0.9653	0.7025	0.6923	0.8492	0.9648	0.5303	0.9333	0.8610	0.9791	0.6280	0.9444
SoM [48]	0.8100	0.9721	0.6335	0.7852	0.8658	0.9745	0.5083	0.7671	0.9225	0.9833	0.3253	0.9250
Ours	0.8798	0.9747	0.5926	0.8540	0.8707	0.9750	0.5059	0.8421	0.9275	0.9853	0.3216	0.9883

Method	Spin				Teddy				Mean			
	CLIP-I \uparrow	CLIP-T \uparrow	LPIPS \downarrow	PCK-T \uparrow	CLIP-I \uparrow	CLIP-T \uparrow	LPIPS \downarrow	PCK-T \uparrow	CLIP-I \uparrow	CLIP-T \uparrow	LPIPS \downarrow	PCK-T \uparrow
T-NeRF [9]	0.8328	0.9565	0.5714	-	0.8242	0.9541	0.6337	-	0.8604	0.9688	0.5662	-
HyperNeRF [37]	0.8498	0.9594	0.4905	0.1149	0.8836	0.9630	0.5801	0.7749	0.8750	0.9714	0.5261	0.3060
Deformable 3DGS [56]	0.7457	0.9712	0.5962	0.1881	0.7791	0.9629	0.7601	0.2478	0.7965	0.9721	0.7163	0.2001
Marbles [44]	0.8272	0.9527	0.5761	0.6230	0.8097	0.9606	0.6671	0.9039	0.8305	0.9645	0.6208	0.8194
SoM [48]	0.8510	0.9585	0.3832	0.9073	0.8521	0.9676	0.5630	0.8475	0.8603	0.9712	0.4827	0.8464
Ours	0.8853	0.9658	0.3696	0.9158	0.8902	0.9744	0.5296	0.8807	0.8907	0.9750	0.4639	0.8962

Table 1. Quantitative results of novel view synthesis and tracking on the iPhone dataset [9]. Cells are highlighted as: **best**, **second best**, and **third best**.

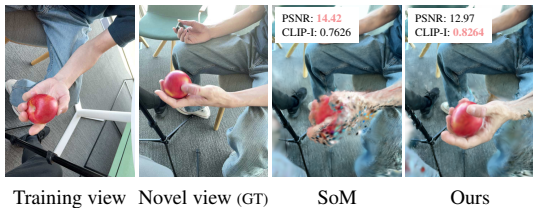


Figure 2. Visualizations of reference images and rendered results. Both SoM and ours resulted in some misalignment w.r.t. the ground truth: while SoM’s result is noticeably broken, it achieves a higher PSNR due to the hand transparency; ours maintains integrity in both geometry and appearance, yet has a lower PSNR. We found that evaluating reconstruction quality using a perceptual metric (*i.e.*, CLIP-I [62]) aligns more with human perception.

for evaluation. We use the provided camera parameters for both datasets.

Evaluation metrics. For the iPhone dataset, given the highly ill-posed nature of monocular dynamic 3D scene reconstruction and the significant perspective differences between training and test views, predicting the precise absolute positions of a scene can be quite challenging, even for humans. As illustrated in Fig. 2, predicting the exact position of the hand can be difficult, leading to a certain degree of misalignment between the reconstructed results and the ground truth. Under such misalignment, pixel-level metrics like PSNR may not always accurately reflect the quality of the reconstruction. To mitigate such impact, we propose the use of two perceptual metrics: CLIP-I to measure the cosine similarity between the CLIP embeddings [40] of the rendered image and the ground truth, and CLIP-T to compare the similarity between frames with certain interval to assess temporal consistency, following the work in 4D gen-

Method	PSNR \uparrow	SSIM \uparrow	LPIPS \downarrow
T-NeRF [9]	23.241	0.7462	0.11450
HyperNeRF [37]	23.237	0.7516	0.10794
Deformable 3DGS [56]	16.483	0.3741	0.33956
Marbles [44]	23.238	0.7541	0.09603
SoM [48]	23.290	0.7565	0.09374
Ours	23.400	0.7621	0.09370

Table 2. Quantitative results of novel view synthesis on the Nvidia dataset [43].

eration [58]. LPIPS [61] is also a perceptual metric, but it can still be influenced by the misalignment, thus we show it as a reference. Additionally, the evaluation protocol in [9] applies co-visibility masks to exclude regions visible in only a few training images. However, we observed that a large portion of the foreground dynamic object is masked out by this co-visibility mask, which does not properly reflect the quality of novel view synthesis, particularly in occluded regions. Consequently, we apply the co-visibility mask only to the background. We also adopt percentage of correctly transferred keypoints (PCK-T) as the metric to evaluate long-range tracking from training views, as in [9].

For the Nvidia dataset, since the perspectives of training and testing are quite similar, the misalignment is minimal. Thus, we follow previous works and use PSNR, SSIM, and LPIPS as metrics.

4.1. Results

We first evaluate our method on the iPhone dataset [9], which contains substantial occlusions and complex motions. Tab. 1 presents quantitative comparisons of our method with existing NeRF-based [9, 37] and 3DGS-based [44, 48, 56] approaches. We exclude MoSca [15]

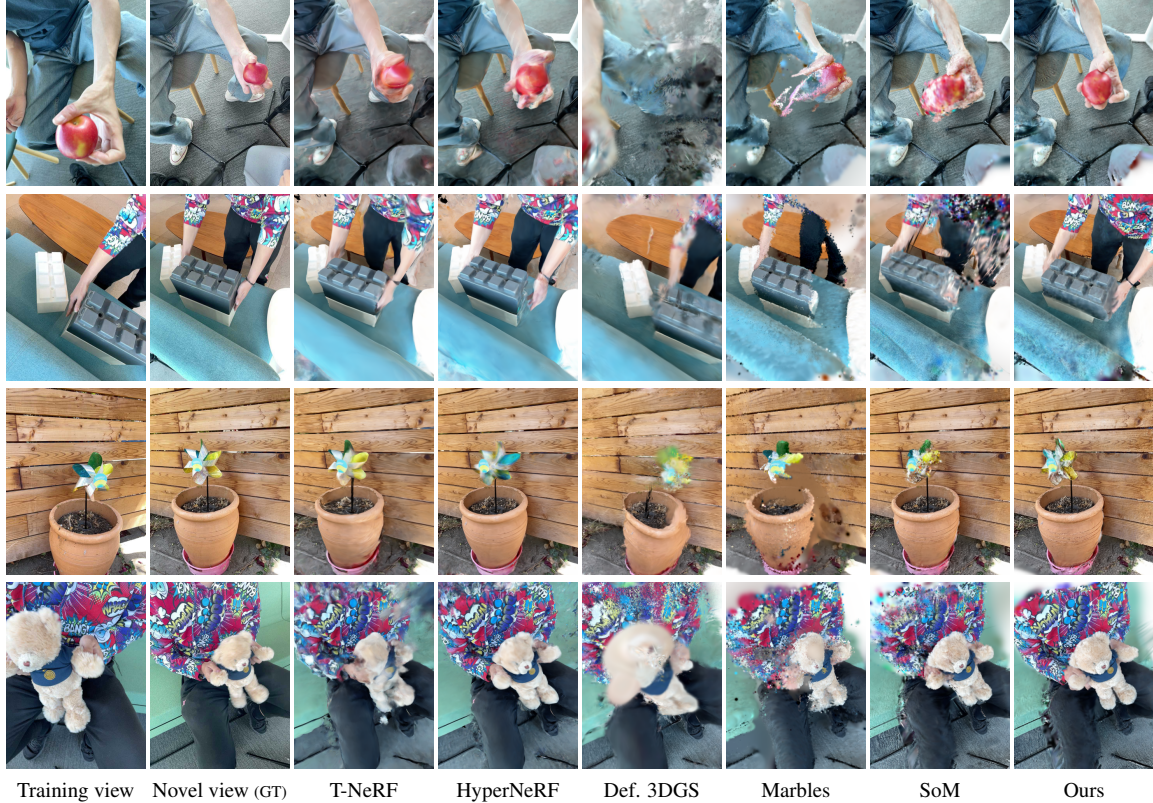


Figure 3. Qualitative results of novel view synthesis on the iPhone dataset [9]. From the top are “Apple”, “Block”, “Paper-windmill”, and “Teddy”.

from the comparisons because its code is not yet publicly available (as of Nov. 2024), and the descriptions in the paper are insufficient for reimplementation. However, we conduct ablation studies against a MoSca-like variant in Sec. 4.2. It is important to note that temporal consistency can be achieved even with poor image quality (*i.e.*, producing the same image for all timesteps). Therefore, CLIP-T must be considered alongside CLIP-I and LPIPS for a comprehensive assessment. Our method outperforms existing approaches overall by a large margin in both novel view synthesis and tracking.

The qualitative comparisons of novel view synthesis are shown in Fig. 3. Our method demonstrates its superiority to previous 3DGS-based approaches, which either overfit to training views (*i.e.*, Def. 3DGS) or suffer from geometry collapse (*i.e.*, Marbles and SoM). Compared to NeRF-based methods, our method performs better, except for the “Block” scene. Since the hand on the right side of the novel view image is completely occluded in the training view and can move independently from other visible parts, it is nearly impossible to accurately infer its exact motion. Given the high degree of freedom in unstructured Gaussian primitives, 3DGS-based methods struggle in such cases with little direct supervision. In contrast, NeRF-based methods are in-

herently better at interpolation with MLPs as representation, leading to more reasonable results. However, their drawback is that they tend to produce blurry results (*i.e.*, “Teddy”) corresponding to high LPIPS.

The qualitative comparisons of temporal consistency are presented in Fig. 4. Our method better maintains temporal consistency, even outperforming NeRF-based approaches. This highlights the effectiveness of our deformation representation in constraining unstructured 3D Gaussians.

We show the quantitative results on the Nvidia dataset [43] in Tab. 2. Our method achieves competitive results compared to previous approaches, demonstrating its ability to handle a wide range of scenes.

4.2. Ablation studies

We conduct ablation studies on our method using the “Spin” scene from the iPhone dataset [9]. The quantitative results are shown in Tab. 3. For a fair comparison, all variants use the same number of nodes. Regarding evaluation metrics, LPIPS involves pixel-level calculations and is therefore sensitive to misalignment as mentioned earlier. PCK-T is calculated from the training view, which may not fully reflect reconstruction quality. Thus, to explore the impact on the quality of novel view synthesis, our ablation studies

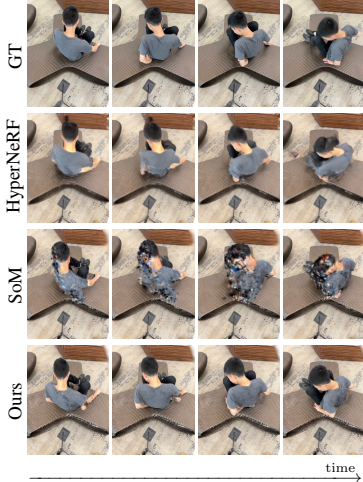


Figure 4. Qualitative comparison of temporal consistency at novel view on the iPhone dataset [9]. The time interval of adjacent images is ten frames.

Method	CLIP-I \uparrow	CLIP-T \uparrow	LPIPS \downarrow	PCK-T \uparrow
Baseline	0.8677	0.9554	0.3746	0.9296
+ Motion bases	0.8736	0.9634	0.3656	0.9179
+ Hierarchical structure	0.8753	0.9649	0.3655	0.9184
+ Rigidity loss	0.8851	0.9653	0.3680	0.9156
+ Node densification (Full)	0.8853	0.9658	0.3696	0.9158

Table 3. Ablation studies on the “Spin” scene of the iPhone dataset [9]. “+” denotes that the component is incrementally added to the baseline.

primarily focus on CLIP-I and CLIP-T metrics.

Baseline. We first implement a MoSca-like [15] baseline with a single level of nodes, where the motion sequence of each node is modeled independently. The baseline is optimized using Eq. 7, but without \mathcal{L}_{rigid} . Since each node can move independently, the model is more prone to overfitting to the training views, resulting in poor rendering quality.

Motion bases. We incorporate motion bases to model the motion sequence of each node in the baseline. The total number of motion nodes and motion bases is the same as in “+ Hierarchical structure”, but only with one level. Additionally, to align with the configuration, we assign five motion bases to ten nodes rather than sharing them across all nodes. This adjustment significantly improves novel view synthesis performance compared to the baseline.

Hierarchical structure. With the hierarchical structure, performance improves further compared to the previous variant. In particular, the higher CLIP-T indicates that the global constraint introduced by the hierarchical structure enhances spatial and temporal smoothness. We also demonstrate that our hierarchical motion design can achieve a coarse-to-fine motion decomposition in Fig. 5.

Rigidity loss. We found that rigidity loss leads to an im-



Figure 5. Motion decomposition via hierarchical structure. The sequences are rendered at a fixed camera. We extract (a) coarse motion by freezing second-level nodes and (b) fine motion by freezing first-level nodes. It can be observed that (a) models general movements of the arm and the backpack, whereas (b) captures subtle rotations of the backpack and the swing of the straps.

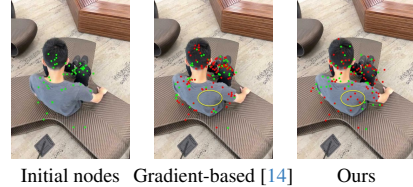


Figure 6. Node densification. The green points represent the initial nodes, while the red points denote nodes added through the densification process. Our densification strategy can add nodes to the regions with few initial nodes (*i.e.*, men’s back, inside yellow circle), and the resulting nodes are more uniform.

provement in performance, especially in terms of CLIP-I. This indicates that rigidity loss is effective in preserving overall geometry and preventing unrealistic distortion.

Node densification. As shown in Fig. 6, our node densification can add nodes to the regions with few nodes. With well-distributed nodes, the interpolation of motion sequence becomes smoother, resulting in an improvement.

5. Conclusion and limitation

We have presented HiMoR, a novel hierarchical motion representation combined with 3D Gaussian representation that significantly improves monocular dynamic 3D reconstruction quality. Utilizing a tree structure, HiMoR represents motions in a coarse-to-fine manner, providing more structured deformation for Gaussians. We have also highlighted the limitations of pixel-level metrics for evaluating monocular dynamic 3D reconstruction and proposed using a more reliable perceptual metric as an alternative.

Similar to other deformation-based approaches, one shortcoming of our method is that it struggles to accurately represent parts that do not exist in the canonical frame, such as newly added objects or newly exposed parts of the scene. Possible solutions to this limitation could include providing a separate branch to handle newly appearing objects, or designing an adaptive canonical space, both of which would present interesting directions for future research.

Acknowledgment. We thank Hiroharu Kato and So-suke Kobayashi for helpful discussions and comments.

References

- [1] Jonathan T. Barron, Ben Mildenhall, Dor Verbin, Pratul P. Srinivasan, and Peter Hedman. Zip-nerf: Anti-aliased grid-based neural radiance fields. In *ICCV*, 2023. 2
- [2] David Charatan, Sizhe Li, Andrea Tagliasacchi, and Vincent Sitzmann. pixelsplat: 3d gaussian splats from image pairs for scalable generalizable 3d reconstruction. In *CVPR*, 2024. 2
- [3] Yiwen Chen, Zilong Chen, Chi Zhang, Feng Wang, Xiaofeng Yang, Yikai Wang, Zhongang Cai, Lei Yang, Huaping Liu, and Guosheng Lin. Gaussianeditor: Swift and controllable 3d editing with gaussian splatting. In *CVPR*, 2024. 2
- [4] Yuedong Chen, Haofei Xu, Chuanxia Zheng, Bohan Zhuang, Marc Pollefeys, Andreas Geiger, Tat-Jen Cham, and Jianfei Cai. Mvsplat: Efficient 3d gaussian splatting from sparse multi-view images. In *ECCV*, 2024. 2
- [5] Carl Doersch, Yi Yang, Mel Vecerik, Dilara Gokay, Ankush Gupta, Yusuf Aytar, Joao Carreira, and Andrew Zisserman. TAPIR: Tracking any point with per-frame initialization and temporal refinement. In *CVPR*, pages 10061–10072, 2023. 4, 5, 11
- [6] Daniel Duckworth, Peter Hedman, Christian Reiser, Peter Zhizhin, Jean-François Thibert, Mario Lučić, Richard Szeliski, and Jonathan T. Barron. Smerf: Streamable memory efficient radiance fields for real-time large-scene exploration. *ACM Trans. Graph.*, 43(4), 2024. 2
- [7] Zhiwen Fan, Kevin Wang, Kairun Wen, Zehao Zhu, Dejia Xu, and Zhangyang Wang. Lightgaussian: Unbounded 3d gaussian compression with 15x reduction and 200+ fps. In *NeurIPS*, 2024. 2
- [8] Sara Fridovich-Keil, Giacomo Meanti, Frederik Rahbæk Warburg, Benjamin Recht, and Angjoo Kanazawa. K-planes: Explicit radiance fields in space, time, and appearance. In *CVPR*, 2023. 2
- [9] Hang Gao, Ruilong Li, Shubham Tulsiani, Bryan Russell, and Angjoo Kanazawa. Monocular dynamic view synthesis: A reality check. In *NeurIPS*, 2022. 2, 5, 6, 7, 8, 11, 12, 15, 16, 17, 18
- [10] Abdullah Hamdi, Luke Melas-Kyriazi, Jinjie Mai, Guocheng Qian, Ruoshi Liu, Carl Vondrick, Bernard Ghanem, and Andrea Vedaldi. Ges: Generalized exponential splatting for efficient radiance field rendering. In *CVPR*, pages 19812–19822, 2024. 2
- [11] Ayaan Haque, Matthew Tancik, Alexei Efros, Aleksander Holynski, and Angjoo Kanazawa. Instruct-nerf2nerf: Editing 3d scenes with instructions. In *ICCV*, 2023. 2
- [12] Liangxiao Hu, Hongwen Zhang, Yuxiang Zhang, Boyao Zhou, Boning Liu, Shengping Zhang, and Liqiang Nie. Gaussianavatar: Towards realistic human avatar modeling from a single video via animatable 3d gaussians. In *CVPR*, 2024. 2
- [13] Binbin Huang, Zehao Yu, Anpei Chen, Andreas Geiger, and Shenghua Gao. 2d gaussian splatting for geometrically accurate radiance fields. In *SIGGRAPH 2024 Conference Papers*. Association for Computing Machinery, 2024. 2
- [14] Y. Huang, Y. Sun, Z. Yang, X. Lyu, Y. Cao, and X. Qi. Scgs: Sparse-controlled gaussian splatting for editable dynamic scenes. In *CVPR*, pages 4220–4230, 2024. 5, 8
- [15] Lei Jiahui, Weng Yijia, Harley Adam, Guibas Leonidas, and Daniilidis Kostas. Mosca: Dynamic gaussian fusion from casual videos via 4d motion scaffolds. *arXiv preprint arXiv:2405.17421*, 2024. 1, 2, 3, 4, 5, 6, 8
- [16] Zijie Jiang, Tianhan Xu, and Hiroharu Kato. Rethinking directional parameterization in neural implicit surface reconstruction. In *ECCV*, 2024. 2
- [17] Bernhard Kerbl, Georgios Kopanas, Thomas Leimkühler, and George Drettakis. 3d gaussian splatting for real-time radiance field rendering. *ACM Transactions on Graphics*, 42(4), 2023. 1, 2, 3, 5, 11
- [18] Shakiba Kheradmand, Daniel Rebain, Gopal Sharma, Weiwei Sun, Jeff Tseng, Hossam Isack, Abhishek Kar, Andrea Tagliasacchi, and Kwang Moo Yi. 3d gaussian splatting as markov chain monte carlo. *arXiv preprint arXiv:2404.09591*, 2024. 2
- [19] Diederik Kingma and Jimmy Ba. Adam: A method for stochastic optimization. In *International Conference on Learning Representations (ICLR)*, San Diego, CA, USA, 2015. 11
- [20] Sosuke Kobayashi, Eiichi Matsumoto, and Vincent Sitzmann. Decomposing nerf for editing via feature field distillation. In *NeurIPS*, 2022. 2
- [21] Agelos Kratimenos, Jiahui Lei, and Kostas Daniilidis. Dynmf: Neural motion factorization for real-time dynamic view synthesis with 3d gaussian splatting. In *ECCV*, 2024. 2, 3
- [22] Tianye Li, Miroslava Slavcheva, Michael Zollhoefer, Simon Green, Christoph Lassner, Changil Kim, Tanner Schmidt, S. Lovegrove, Michael Goesele, Richard A. Newcombe, and Zhaoyang Lv. Neural 3d video synthesis from multi-view video. In *CVPR*, 2022. 2
- [23] Zhengqi Li, Simon Niklaus, Noah Snavely, and Oliver Wang. Neural scene flow fields for space-time view synthesis of dynamic scenes. In *CVPR*, 2021. 2
- [24] Zhan Li, Zhang Chen, Zhong Li, and Yi Xu. Spacetime gaussian feature splatting for real-time dynamic view synthesis. In *CVPR*, pages 8508–8520, 2024. 2
- [25] Chen-Hsuan Lin, Wei-Chiu Ma, Antonio Torralba, and Simon Lucey. Barf: Bundle-adjusting neural radiance fields. In *ICCV*, 2021. 2
- [26] Qingming Liu, Yuan Liu, Jiepeng Wang, Xianqiang Lyv, Peng Wang, Wenping Wang, and Junhui Hou. Modgs: Dynamic gaussian splatting from casually-captured monocular videos. *arXiv preprint arXiv:2406.00434*, 2024. 1, 2
- [27] Tao Lu, Mulin Yu, Linning Xu, Yuanbo Xiangli, Limin Wang, Dahua Lin, and Bo Dai. Scaffold-gs: Structured 3d gaussians for view-adaptive rendering. In *CVPR*, pages 20654–20664, 2024. 2
- [28] Jonathon Luiten, Georgios Kopanas, Bastian Leibe, and Deva Ramanan. Dynamic 3d gaussians: Tracking by persistent dynamic view synthesis. In *3DV*, 2024. 4, 5
- [29] Jonathon Luiten, Georgios Kopanas, Bastian Leibe, and Deva Ramanan. Dynamic 3d gaussians: Tracking by persistent dynamic view synthesis. In *3DV*, 2024. 1, 2
- [30] Ben Mildenhall, Pratul P. Srinivasan, Matthew Tancik, Jonathan T. Barron, Ravi Ramamoorthi, and Ren Ng. Nerf:

- Representing scenes as neural radiance fields for view synthesis. In *ECCV*, 2020. 2
- [31] Nicolas Moenne-Loccoz, Ashkan Mirzaei, Or Perel, Riccardo de Lutio, Janick Martinez Esturo, Gavriel State, Sanja Fidler, Nicholas Sharp, and Zan Gojcic. 3D Gaussian Ray Tracing: Fast tracing of particle scenes. *ACM Transactions on Graphics and SIGGRAPH Asia*, 2024. 2
- [32] Thomas Müller, Alex Evans, Christoph Schied, and Alexander Keller. Instant neural graphics primitives with a multi-resolution hash encoding. *ACM Trans. Graph.*, 41(4):102:1–102:15, 2022. 2
- [33] KL Navaneet, Kossar Pourahmadi Meibodi, Soroush Abbasi Koohpayegani, and Hamed Pirsiavash. Compgs: Smaller and faster gaussian splatting with vector quantization. In *ECCV*, 2024. 2
- [34] Richard A. Newcombe, Dieter Fox, and Steven M. Seitz. Dynamicfusion: Reconstruction and tracking of non-rigid scenes in real-time. In *CVPR*, pages 343–352, 2015. 4
- [35] Atsuhiko Noguchi, Umar Iqbal, Jonathan Tremblay, Tatsuya Harada, and Orazio Gallo. Watch it move: Unsupervised discovery of 3d joints for re-posing of articulated objects. In *CVPR*, pages 3677–3687, 2022. 2
- [36] Keunhong Park, Utkarsh Sinha, Jonathan T. Barron, Sofien Bouaziz, Dan B Goldman, Steven M. Seitz, and Ricardo Martin-Brualla. Nerfies: Deformable neural radiance fields. In *CVPR*, 2021. 2
- [37] Keunhong Park, Utkarsh Sinha, Peter Hedman, Jonathan T. Barron, Sofien Bouaziz, Dan B Goldman, Ricardo Martin-Brualla, and Steven M. Seitz. Hypernerf: A higher-dimensional representation for topologically varying neural radiance fields. *ACM Trans. Graph.*, 40(6), 2021. 2, 6, 12
- [38] Albert Pumarola, Enric Corona, Gerard Pons-Moll, and Francesc Moreno-Noguer. D-NeRF: Neural Radiance Fields for Dynamic Scenes. In *CVPR*, 2020. 2
- [39] Zhiyin Qian, Shaofei Wang, Marko Mihajlovic, Andreas Geiger, and Siyu Tang. 3dgs-avatar: Animatable avatars via deformable 3d gaussian splatting. In *CVPR*, 2024. 2
- [40] Alec Radford, Jong Wook Kim, Chris Hallacy, Aditya Ramesh, Gabriel Goh, Sandhini Agarwal, Girish Sastry, Amanda Askell, Pamela Mishkin, Jack Clark, Gretchen Krueger, and Ilya Sutskever. Learning transferable visual models from natural language supervision. In *International Conference on Machine Learning*, pages 8748–8763, 2022. 6, 11
- [41] Johannes Lutz Schönberger and Jan-Michael Frahm. Structure-from-motion revisited. In *CVPR*, 2016. 5, 11
- [42] Zhijing Shao, Zhaolong Wang, Zhuang Li, Duotun Wang, Xiangru Lin, Yu Zhang, Mingming Fan, and Zeyu Wang. SplattingAvatar: Realistic Real-Time Human Avatars with Mesh-Embedded Gaussian Splatting. In *CVPR*, 2024. 2
- [43] Jae Shin Yoon, Kihwan Kim, Orazio Gallo, Hyun Soo Park, and Jan Kautz. Novel View Synthesis of Dynamic Scenes With Globally Coherent Depths From a Monocular Camera. In *CVPR*, pages 5335–5344, 2020. 5, 6, 7, 11, 12
- [44] Colton Stearns, Adam W Harley, Mikaela Uy, Florian Dubost, Federico Tombari, Gordon Wetzstein, and Leonidas Guibas. Dynamic gaussian marbles for novel view synthesis of casual monocular videos. In *SIGGRAPH Asia 2024 Conference Papers*, pages 1–11, 2024. 1, 2, 5, 6, 11, 12
- [45] Stanislaw Szymanowicz, Christian Rupprecht, and Andrea Vedaldi. Splatter image: Ultra-fast single-view 3d reconstruction. In *CVPR*, 2024. 2
- [46] Dor Verbin, Peter Hedman, Ben Mildenhall, Todd Zickler, Jonathan T. Barron, and Pratul P. Srinivasan. Ref-NeRF: Structured view-dependent appearance for neural radiance fields. In *CVPR*, 2022. 2
- [47] Liao Wang, Jiakai Zhang, Xinhang Liu, Fuqiang Zhao, Yanshun Zhang, Yingliang Zhang, Minye Wu, Jingyi Yu, and Lan Xu. Fourier plencotrees for dynamic radiance field rendering in real-time. In *CVPR*, pages 13524–13534, 2022. 2
- [48] Qianqian Wang, Vickie Ye, Hang Gao, Jake Austin, Zhengqi Li, and Angjoo Kanazawa. Shape of motion: 4d reconstruction from a single video. *arXiv preprint arXiv:2407.13764*, 2024. 1, 2, 3, 4, 5, 6, 11, 12
- [49] Shizun Wang, Xingyi Yang, Qiuhong Shen, Zhenxiang Jiang, and Xinchao Wang. Gflow: Recovering 4d world from monocular video. *arXiv preprint arXiv:2405.18426*, 2024. 1, 2
- [50] Zhou Wang, Alan C Bovik, Hamid R Sheikh, and Eero P Simoncelli. Image quality assessment: from error visibility to structural similarity. *IEEE transactions on image processing*, 13(4):600–612, 2004. 11
- [51] Chung-Yi Weng, Brian Curless, Pratul P. Srinivasan, Jonathan T. Barron, and Ira Kemelmacher-Shlizerman. HumanNeRF: Free-viewpoint rendering of moving people from monocular video. In *CVPR*, pages 16210–16220, 2022. 2
- [52] GuanJun Wu, Taoran Yi, Jiemin Fang, Lingxi Xie, Xiaopeng Zhang, Wei Wei, Wenyu Liu, Qi Tian, and Xinggang Wang. 4d gaussian splatting for real-time dynamic scene rendering. In *CVPR*, pages 20310–20320, 2024. 1, 2
- [53] Tianhan Xu and Tatsuya Harada. Deforming radiance fields with cages. In *ECCV*, 2022. 2
- [54] Jinyu Yang, Mingqi Gao, Zhe Li, Shang Gao, Fangjing Wang, and Feng Zheng. Track anything: Segment anything meets videos. *arXiv preprint arXiv:2304.11968*, 2023. 5, 11
- [55] Lihe Yang, Bingyi Kang, Zilong Huang, Xiaogang Xu, Jiashi Feng, and Hengshuang Zhao. Depth anything: Unleashing the power of large-scale unlabeled data. In *CVPR*, 2024. 4, 5, 11
- [56] Ziyi Yang, Xinyu Gao, Wen Zhou, Shaohui Jiao, Yuqing Zhang, and Xiaogang Jin. Deformable 3d gaussians for high-fidelity monocular dynamic scene reconstruction. In *CVPR*, 2024. 1, 2, 4, 6, 12
- [57] Mingqiao Ye, Martin Danelljan, Fisher Yu, and Lei Ke. Gaussian grouping: Segment and edit anything in 3d scenes. In *ECCV*, 2024. 2
- [58] Yuyang Yin, DeJia Xu, Zhangyang Wang, Yao Zhao, and Yunchao Wei. 4dgen: Grounded 4d content generation with spatial-temporal consistency. *arXiv preprint arXiv:2312.17225*, 2023. 6
- [59] Alex Yu, Vickie Ye, Matthew Tancik, and Angjoo Kanazawa. pixelNeRF: Neural radiance fields from one or few images. In *CVPR*, 2021. 2

- [60] Zehao Yu, Anpei Chen, Binbin Huang, Torsten Sattler, and Andreas Geiger. Mip-splatting: Alias-free 3d gaussian splatting. In *CVPR*, pages 19447–19456, 2024. 2
- [61] Richard Zhang, Phillip Isola, Alexei A Efros, Eli Shechtman, and Oliver Wang. The unreasonable effectiveness of deep features as a perceptual metric. In *CVPR*, 2018. 6, 11
- [62] Yuyang Zhao, Zhiwen Yan, Enze Xie, Lanqing Hong, Zhen-guo Li, and Gim Hee Lee. Animate124: Animating one image to 4d dynamic scene. *arXiv preprint arXiv:2311.14603*, 2023. 6

A. Additional results

iPhone dataset. We show qualitative comparison of temporal consistency at novel view on the iPhone dataset [9] in Fig. 10, 11, 12, 13. Our method demonstrates better overall temporal consistency.

Nvidia dataset. We show per-scene quantitative results of novel view synthesis on the Nvidia dataset [43] in Tab. 4, and qualitative results in Fig. 7.

Ablation studies. We show qualitative results of ablation studies in Fig. 8.

B. Additional training details

B.1. Loss functions and weights

Here, we provide a detailed explanation for each term of the loss in main text Eq. 7.

RGB loss \mathcal{L}_{rgb} , mask loss \mathcal{L}_{mask} , and depth loss \mathcal{L}_{depth} , ensure that the rendered image, foreground mask, and depth to match their respective ground truth in a pixel-wise manner. The RGB loss \mathcal{L}_{rgb} is a combined MSE (mean squared error) loss, D-SSIM [50] loss, and LPIPS [61] loss between the rendered image and the ground truth, weighted 0.8, 0.2, and 0.01, respectively. Mask loss \mathcal{L}_{mask} computes MSE between rendered mask and the mask predicted via [54] with weight of 1.0. For the depth loss \mathcal{L}_{depth} , we include an MSE term weighted 0.5, and following [48], apply a regularization to the gradient of the rendered depth, weighted 1.0.

The tracking loss \mathcal{L}_{track} supervises the rendered tracks to match the unprojected 2D tracks from [5]. Following [48], we compute \mathcal{L}_{track} as a combination of $\mathcal{L}_{track-2d}$ and $\mathcal{L}_{track-depth}$, with respective weights of 2.0 and 0.1. $\mathcal{L}_{track-2d}$ is the MSE loss between rendered 2D tracks and the 2D tracks from [5] on normalized pixel coordinates, while $\mathcal{L}_{track-depth}$ is the MSE loss between the reprojected depths of the rendered tracks and the metric aligned depths from [55].

The rigidity loss \mathcal{L}_{rigid} is calculated as:

$$\mathcal{L}_{rigid} = \sum_{i \in \mathcal{N}} \sum_{j \in \text{KNN}(i)} (\|\mathbf{x}_{i,t} - \mathbf{x}_{j,t}\| - \|\mathbf{x}_{i,t+\Delta} - \mathbf{x}_{j,t+\Delta}\| + \|\mathbf{T}_{j,t}^{-1} \mathbf{x}_{i,t} - \mathbf{T}_{j,t+\Delta}^{-1} \mathbf{x}_{i,t+\Delta}\|), \quad (8)$$

where $\mathbf{x}_{*,t}$ and $\mathbf{T}_{*,t}$ denote node’s position at time t and its deformation from the canonical frame to time t , respectively. Δ denotes time interval within the sampled batch. The set of nodes is denoted by \mathcal{N} , while $\text{KNN}(i)$ refers to the K -nearest neighbors of the i^{th} node, determined by curve distance. The initial weight of \mathcal{L}_{rigid} for first-level nodes is 0.5. Once second-level nodes are activated, the weight for first-level nodes is increased to 2.5, while second-level nodes are assigned a weight of 0.5.

We also include regularization terms for the acceleration of motion bases, the acceleration of rendered tracks, and the scale of Gaussians as [48], with respective weights of 0.1, 2.0, and 0.01. In addition, the radius of nodes are regularized to be no larger than the average distance to its three nearest neighbors. The weight of this regularization is set to 0.0001.

B.2. Optimization

We use Adam [19] to optimize HiMoR and Gaussians in canonical frame jointly. The learning rates for mean, opacity, scale, rotation, and color of each Gaussian are set to 1.6×10^{-4} , 1×10^{-2} , 5×10^{-3} , 1×10^{-3} , and 1×10^{-2} , respectively. The adaptive density control of Gaussians proposed in original 3DGS paper [17] is also applied. The learning rate for motion bases is set to 1.6×10^{-4} . The learning rates for position, radius, and motion coefficients of each node are set to 1.6×10^{-5} , 5×10^{-4} , and 1×10^{-2} , respectively. We train our method using a single V100 GPU with 32GB of VRAM. The total training time is approximately 3 – 6 hours for the iPhone dataset [9], and about 1 hour for the Nvidia dataset [43].

C. Evaluation details

For iPhone dataset [9], we use the preprocessed dataset provided by [48]. For Nvidia dataset [43], we use scripts provided by [48] to generate foreground masks, 2D tracks, and monocular depth maps. The monocular depth maps are aligned with per-frame scale and shift factor computed using the point cloud estimated by running COLMAP [41] on all 12 calibrated cameras as [44]. The results of each baseline are produced using the respective public code with its original settings.

D. Formulation of CLIP-I and CLIP-T

CLIP-I is the cosine similarity between the CLIP embeddings [40] of the rendered image and the ground truth, while

Method	Balloon1			Balloon2			Jumping			Playground		
	PSNR↑	SSIM↑	LPIPS↓	PSNR↑	SSIM↑	LPIPS↓	PSNR↑	SSIM↑	LPIPS↓	PSNR↑	SSIM↑	LPIPS↓
T-NeRF [9]	23.152	0.7498	0.11402	23.475	0.8322	0.09172	20.011	0.6922	0.15557	16.902	0.5438	0.20163
HyperNeRF [37]	22.576	0.7354	0.09916	23.933	0.8501	0.07770	20.279	0.7148	0.14790	16.521	0.5283	0.20321
Deformable 3DGS [56]	15.912	0.2753	0.46370	15.126	0.3071	0.41394	16.685	0.4525	0.34131	12.878	0.3193	0.37822
Marbles [44]	23.377	0.7843	0.07810	23.422	0.8046	0.08843	19.997	0.6545	0.14920	16.944	0.5757	0.15507
SoM [48]	23.692	0.7919	0.06336	23.037	0.8155	0.07606	19.906	0.6692	0.17004	16.976	0.5745	0.15110
Ours	23.901	0.7978	0.06200	23.483	0.8261	0.07540	20.042	0.6910	0.15978	17.125	0.5784	0.14942
Method	Skating			Truck			Umbrella			Mean		
	PSNR↑	SSIM↑	LPIPS↓	PSNR↑	SSIM↑	LPIPS↓	PSNR↑	SSIM↑	LPIPS↓	PSNR↑	SSIM↑	LPIPS↓
T-NeRF [9]	27.177	0.8937	0.05666	27.363	0.8588	0.06407	24.609	0.6528	0.11780	23.241	0.7462	0.11450
HyperNeRF [37]	27.085	0.9080	0.05555	27.632	0.8663	0.06536	24.631	0.6584	0.10668	23.237	0.7516	0.10794
Deformable 3DGS [56]	19.310	0.5504	0.27465	18.209	0.4334	0.18731	17.263	0.2807	0.31782	16.483	0.3741	0.33956
Marbles [44]	27.488	0.8905	0.05698	27.127	0.8580	0.05558	24.309	0.6714	0.08876	23.238	0.7541	0.09603
SoM [48]	27.530	0.9141	0.05514	27.569	0.8738	0.04830	24.318	0.6567	0.09221	23.290	0.7565	0.09374
Ours	27.561	0.9151	0.05803	27.400	0.8761	0.04862	24.295	0.6504	0.10269	23.401	0.7621	0.09370

Table 4. Quantitative results of novel view synthesis on the Nvidia dataset [43].

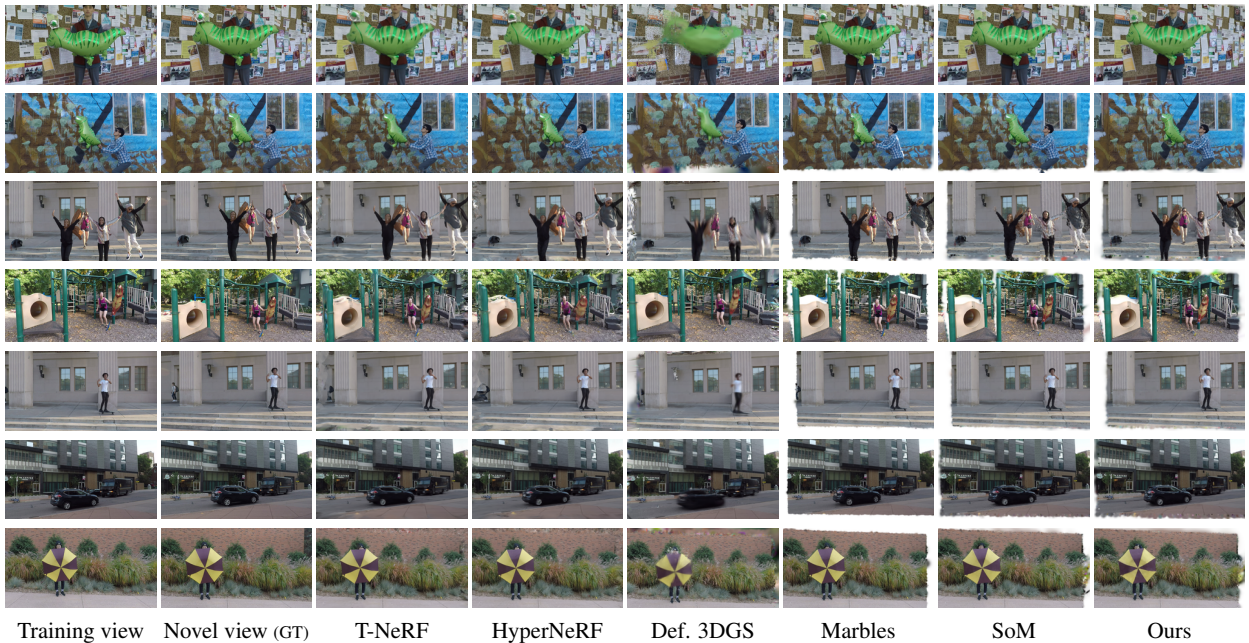


Figure 7. Qualitative results of novel view synthesis on the Nvidia dataset [43]. From the top are “Balloon1”, “Balloon2”, “Jumping”, “Playground”, “Skating”, “Truck”, and “Umbrella”.

CLIP-T is the cosine similarity between frames with certain interval to assess temporal consistency. CLIP-I and CLIP-T are defined as follows:

$$\text{Sim}(\mathbf{v}_i, \mathbf{v}_j) = \frac{\mathbf{v}_i \cdot \mathbf{v}_j}{\|\mathbf{v}_i\| \|\mathbf{v}_j\|}, \quad (9)$$

$$\text{CLIP-I} = \text{Sim}(\mathcal{E}(\hat{I}_t), \mathcal{E}(I_t)), \quad (10)$$

$$\text{CLIP-T} = \text{Sim}(\mathcal{E}(\hat{I}_t), \mathcal{E}(\hat{I}_{t+\Delta})), \quad (11)$$

where $\mathcal{E}(\cdot)$ denotes the CLIP encoder, I_t denotes the ground truth image, and \hat{I}_t refers to the rendered image. Δ specifies the temporal interval between frames for CLIP-T.

E. Additional ablations

We provide additional ablations studies on the number of motion bases and the number of nodes, and an explanation about the number of levels. In our default setting “[10, 5] (ours)”, the initial number of first-level nodes is 50, which increases to approximately 130 after densification. The

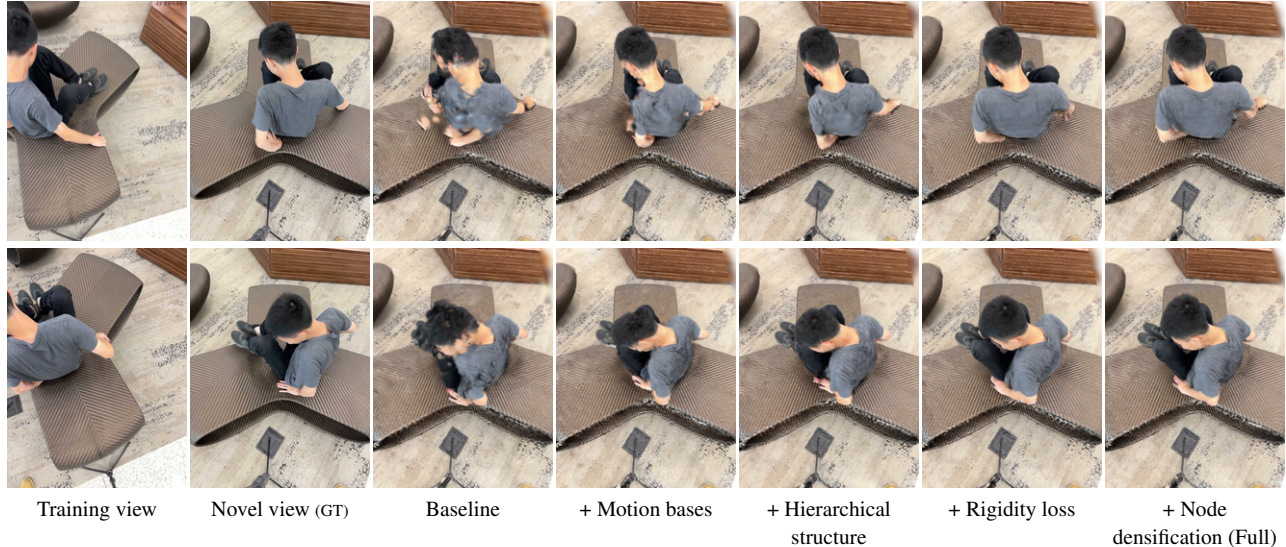


Figure 8. Qualitative results of ablation studies.

Method	CLIP-I \uparrow	CLIP-T \uparrow	LPIPS \downarrow	PCK-T \uparrow
[20, 5]	0.8828	0.9654	0.3627	0.9147
[5, 5]	0.8842	0.9639	0.3696	0.8910
[10, 8]	0.8909	0.9640	0.3667	0.9171
[10, 2]	0.8795	0.9646	0.3675	0.9068
[10, 5] (half)	0.8853	0.9656	0.3664	0.8971
[10, 5] (double)	0.8824	0.9638	0.3646	0.9201
[10, 5] (ours)	0.8853	0.9658	0.3696	0.9158

Table 5. Ablation study on the number of motion bases and nodes. The values inside “[]” represent the number of motion bases for first-level and second-level nodes, respectively. For example, “[10, 5]” indicates that first-level nodes share 10 motion bases, while second-level nodes under the same parent share 5 motion bases. “(half)” denotes that the number of first-level nodes is halved compared to “(ours),” while “(double)” denotes that the number of first-level nodes is doubled compared to “(ours).” Note that, the number of second-level nodes assigned to each first-level node is unchanged.

number of motion bases shared among first-level nodes is set to 10. When activating second-level nodes, 10 nodes are assigned to each first-level node and 5 motion bases are shared among those nodes under the same parent node.

Number of motion bases. We evaluate the sensitivity of performance to the number of motion bases. The results are shown in the first four rows of Tab. 5. Increasing the number of motion bases for first-level nodes has minor impact on overall performance, while reducing motion bases for first-level nodes leads to a loss of detail in the training views, as shown in Fig. 9. For second-level nodes, using more motion bases improves the quality of novel view synthesis

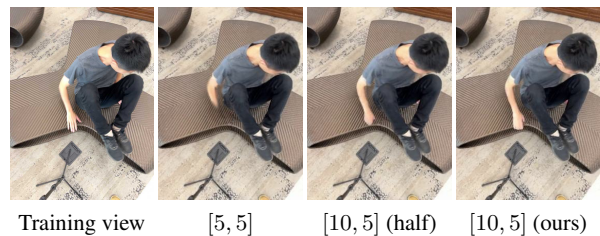


Figure 9. Qualitative results of additional ablation studies on the number of motion bases and nodes. Using fewer motion bases at the first level or fewer nodes in total result in a loss of detail in the training view (*i.e.*, hand).

increased but compromises temporal consistency. When the motion bases for second-level nodes is fewer, it can introduce some subtle distortions, resulting in a lower CLIP-I. Based on the above analysis, we find our default setting to be reasonable.

Number of nodes. We vary the number of first-level nodes to exam the impact of the number of nodes. As predefined number of second-level nodes and motion bases are assigned to each first-level nodes, the number of first-level nodes determines the complexity of HiMoR. The results are shown in “[10, 5] (half)” and “[10, 5] (double)” of Tab. 5. When the number of first-level nodes is halved compared to original settings (ours), PCK-T decreases, suggesting a loss of details in the training views as Fig. 9. Conversely, doubling the number of first-level nodes results in reduced CLIP-I and CLIP-T, likely due to the increased degrees of freedom.

Number of levels. We only use two levels of nodes in our experiment due to the limited number of foreground Gaus-

sian. Current child nodes initialization strategy involves performing K-Means clustering to the relative deformation of the Gaussians within each parent node's radius. However, when the number of Gaussian inside parent node's radius is limited (*i.e.*, less than the number of K-Means clusters), current child nodes initialization strategy may fail. Moreover, increasing the quantity of nodes might not always prove beneficial as the number of Gaussians per node can be significantly small, making the node-based deformation close to per-Gaussian deformation. However, from the algorithmic perspective, we believe that the additional levels of nodes can become more effective in larger scale scenarios or more complex movements.

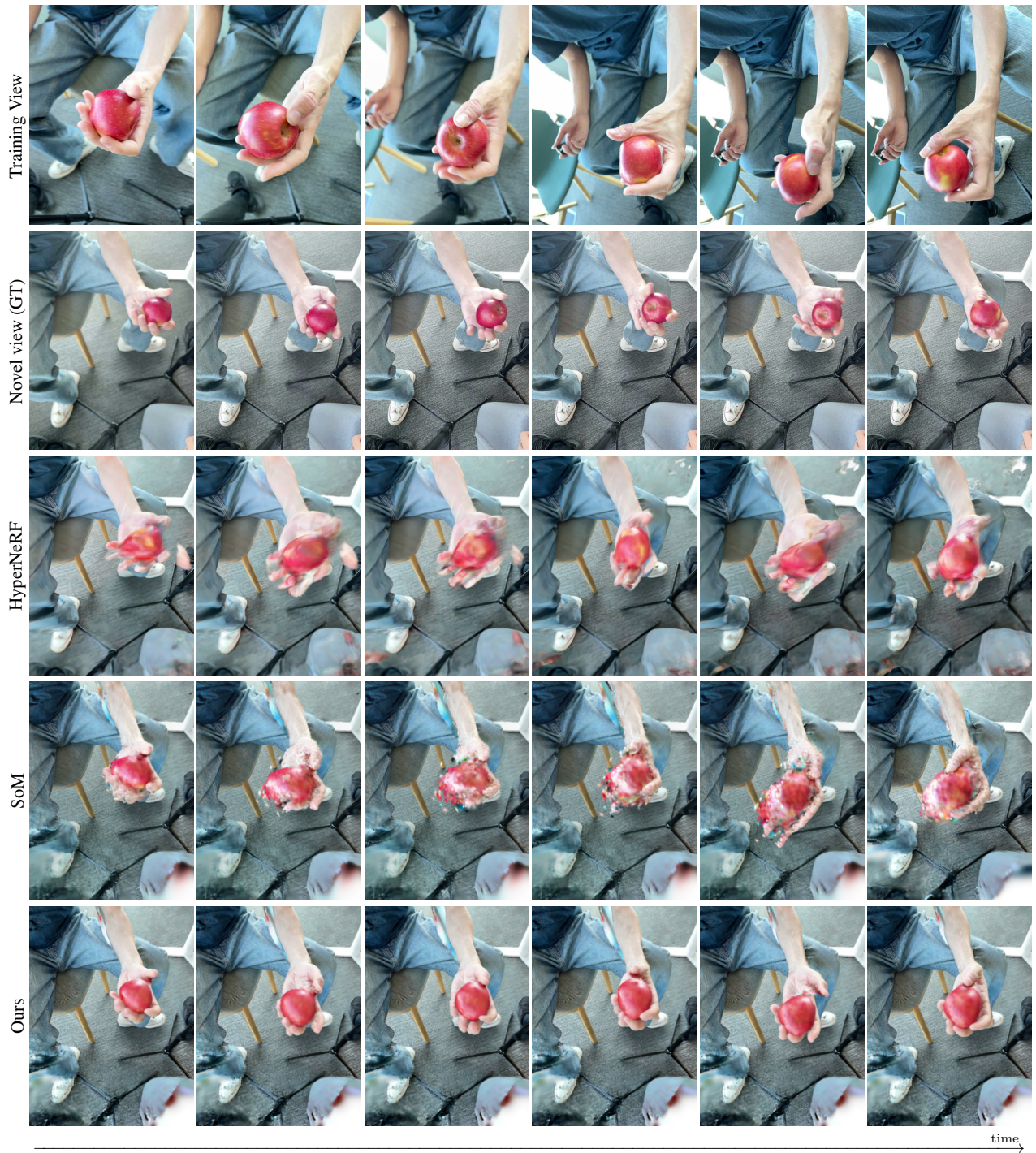


Figure 10. Qualitative comparison of temporal consistency at novel view on the scene “Apple” of iPhone dataset [9]. The time interval of adjacent images is ten frames.

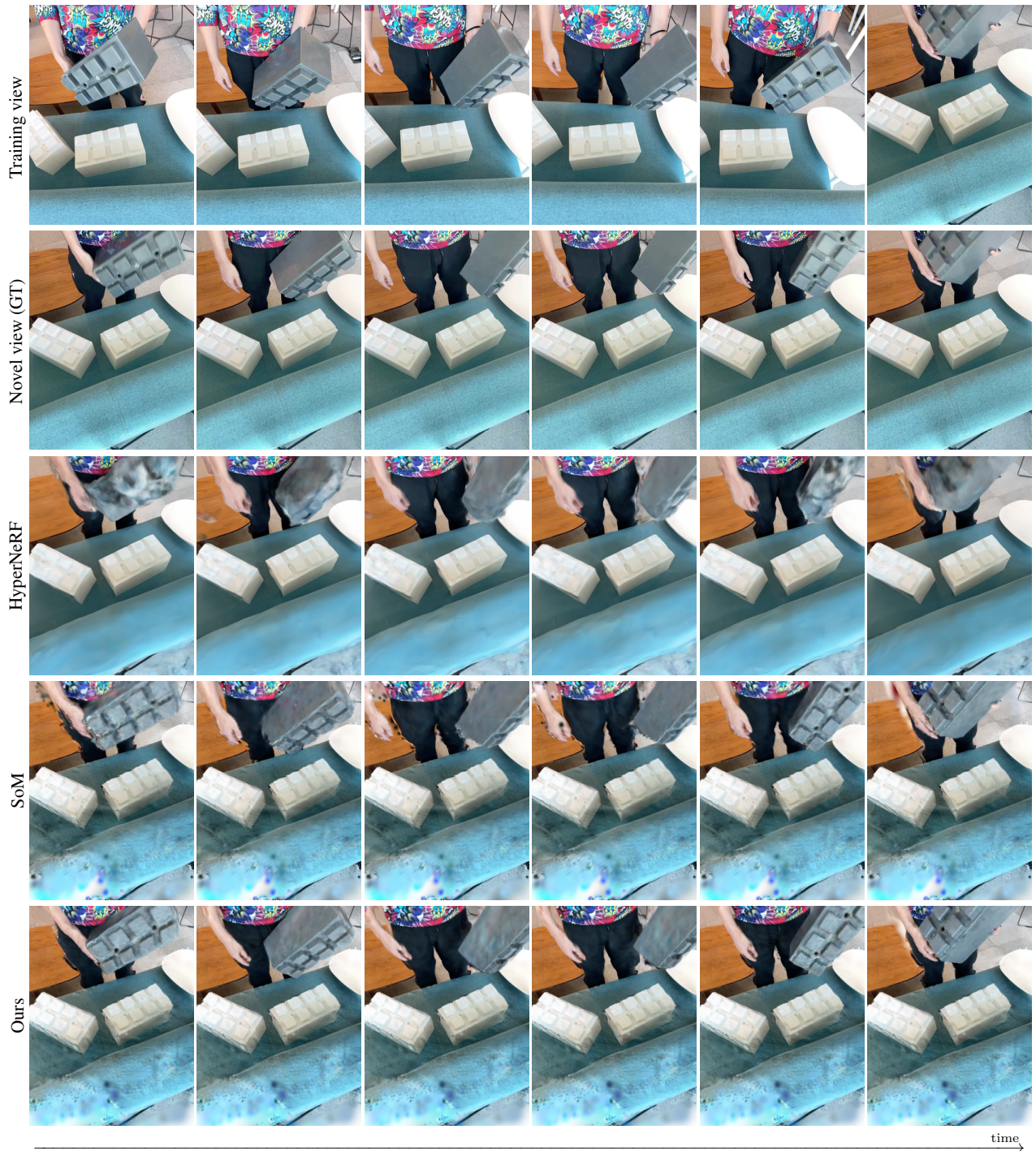


Figure 11. Qualitative comparison of temporal consistency at novel view on the scene “Block” of iPhone dataset [9]. The time interval of adjacent images is ten frames.

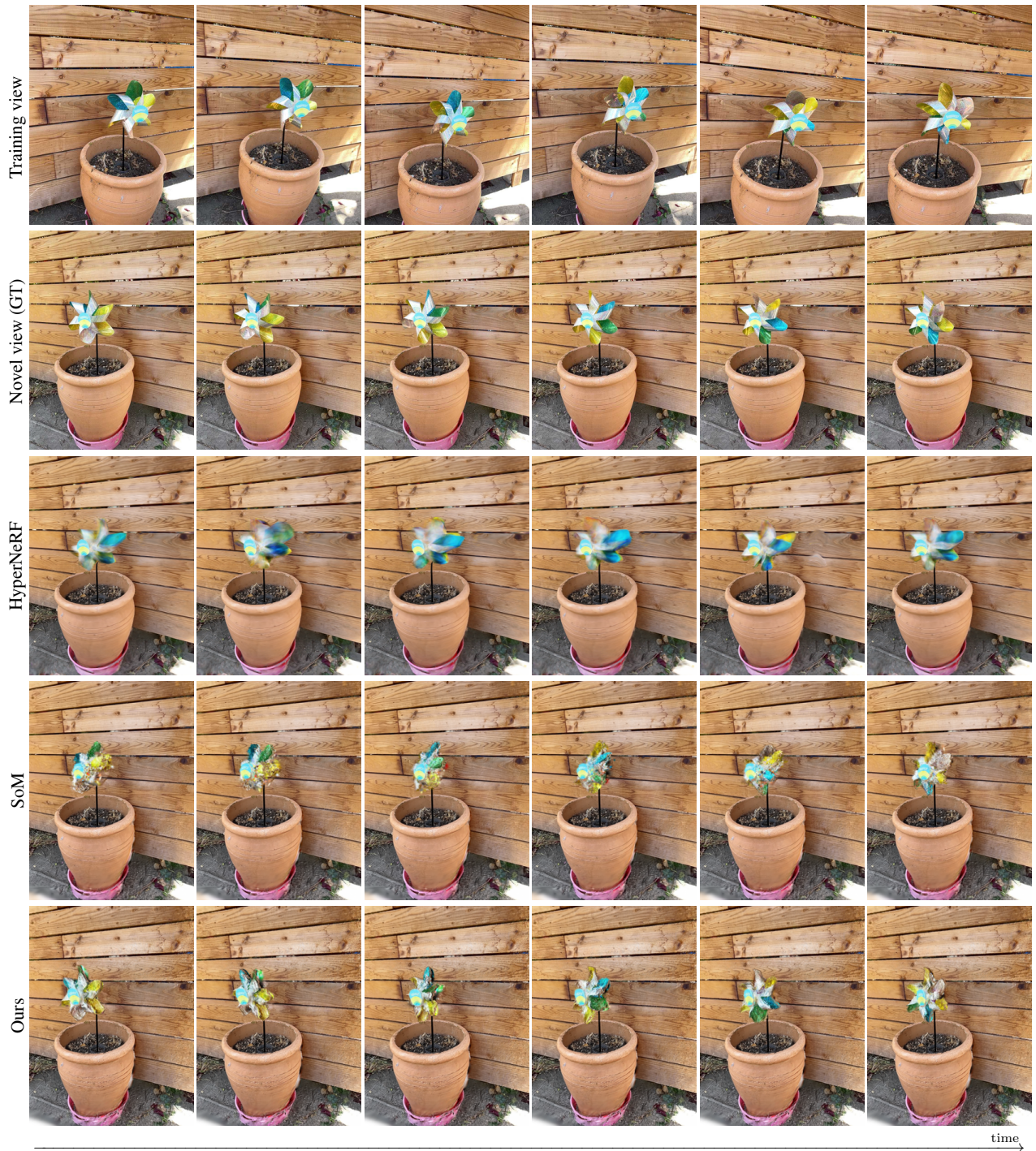


Figure 12. Qualitative comparison of temporal consistency at novel view on the scene “Paper-windmill” of iPhone dataset [9]. The time interval of adjacent images is ten frames.

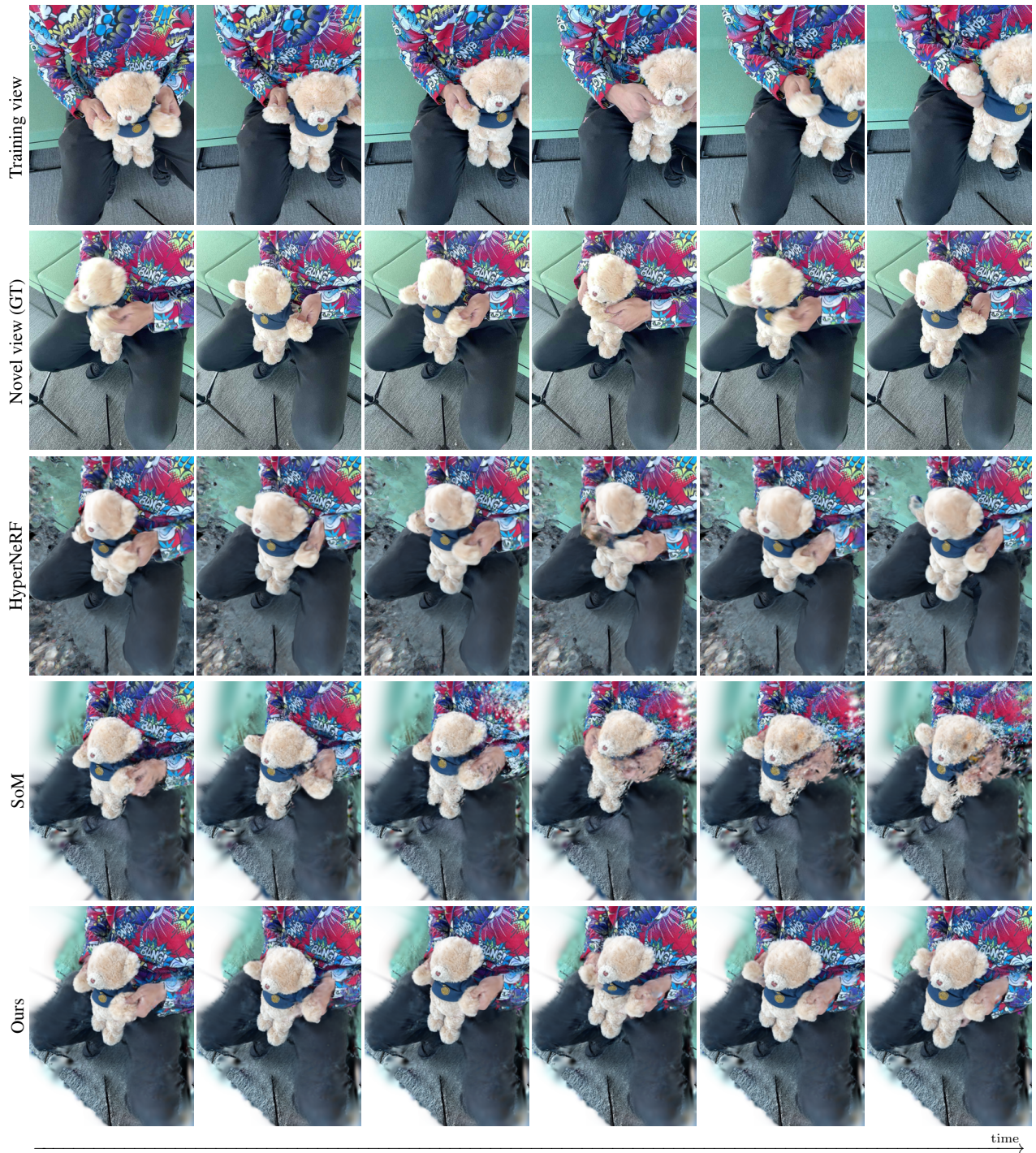


Figure 13. Qualitative comparison of temporal consistency at novel view on the scene “Teddy” of iPhone dataset [9]. The time interval of adjacent images is ten frames.